Monthly Notices
of the
ROYAL ASTRONOMICAL SOCIETY

MNRAS **430,** 1208–1218 (2013)

doi:10.1093/mnras/sts690

Searching for T dwarfs in IC 2391 using methane imaging★†

S. R. Parker‡ and C. G. Tinney

University of New South Wales, Sydney 2052, Australia

Accepted 2012 December 20. Received 2012 December 19; in original form 2012 October 18

ABSTRACT

We have performed a 970 arcmin^2 (1.75 pc^2) survey of the young cluster IC 2391 using the High Acuity Wide field *K*-band Imager on the Very Large Telescope. Observations were made in both the CH_4 and H filters, targeting the methane absorption found in T dwarfs. From our survey of the cluster, five candidate T dwarfs were found. This is substantially smaller than the number that would be found by an equivalent near-infrared broad-band imaging survey, and allowed rapid spectroscopy of all five candidates. Follow-up spectroscopy was carried out using the Folded-port Infrared Echellette on Magellan. These spectra confirm that none of these objects are T dwarfs. This negative result emphasizes the critical importance of follow-up spectroscopy for *any* photometrically selected candidates, even those from methane imaging. Simulations of the photometric data set, combined with data for known IC 2391 members, imply that the power-law mass function in IC 2391 between 0.003 and 0.13 $M_\odot$ has a slope of $\alpha < 1.7$.

Key words: brown dwarfs – stars: low-mass.

1 INTRODUCTION

Brown dwarfs are intrinsically interesting objects to find and study as they provide a unique insight into the star formation process. Their extremely low temperatures (e.g. Lucas et al. 2010; Liu et al. 2011) combined with the fact that they are directly observable make them an important tool in constraining evolutionary models for star formation (Chabrier et al. 2000; Allard et al. 2001; Baraffe et al. 2003). Use of these models to determine masses of known brown dwarfs, which extend down to planetary masses, then provides information on key astrophysical issues such as the minimum mass for star formation.

However, for a brown dwarf's mass to be determined from models, its age must be known. A key method of adding to this sample is to search for brown dwarfs in clusters, where ages of their members are known. For such searches, young, nearby clusters are an obvious target. In this paper, we describe one such search of the cluster IC 2391.

With a distance of 146 ± 5 pc (Robichon et al. 1999), and age of 53 ± 5 Myr (Barrado y Navascués, Stauffer & Patten 1999), IC 2391 is well suited to an infrared survey searching for brown dwarfs. Because of its young age, potential brown dwarf members would be more luminous than those located in an older cluster like the Hyades (age ∼600 Myr). Additionally, IC 2391's compact size on the sky (∼4.9 deg^2; Kharchenko et al. 2005) makes it possible to survey a large fraction of the cluster in a short time.

Previous surveys of IC 2391 have uncovered many cluster members, some with masses (derived from evolutionary models) extending into the brown dwarf regime. One of the first surveys of the cluster, performed by Rolleston & Byrne (1997), reported probable membership of 17 stars, with a further 85 classified as possible members. Barrado y Navascués et al. (2001) carried out an optical and infrared survey, classifying 50 objects as members and 82 as possible members of the cluster. Building on this, Barrado y Navascués, Stauffer & Jayawardhana (2004) obtained optical spectra of 44 member candidates, confirming 33 as members. However, no planetary mass brown dwarfs ($M < 13\,M_J$)[1] have yet been found in IC 2391, and correspondingly nothing is known about the shape of the cluster mass function down to this mass. The aim of this survey was to address this issue.

The particular technique used for our search was methane imaging (Tinney et al. 2005). This uses differential imaging techniques to target methane absorption in the near-infrared, a feature that is exhibited by only the coldest brown dwarfs, spectral types T and Y (Burgasser et al. 2006; Kirkpatrick et al. 2012). By searching for flux differences between a methane (CH_4) filter and an H filter image, this absorption is readily detected.[2]

★ Based on observations collected at the European Organisation for Astronomical Research in the Southern hemisphere, Chile [082.C-0585(A)].

† This paper includes data gathered with the 6.5-m Magellan Telescopes located at Las Campanas Observatory, Chile.

‡ E-mail: sparker@phys.unsw.edu.au

[1] The minimum mass for deuterium burning, 13 M_J, has been the proposed planetary mass limit since the IAU Symposium in 2003 (Boss et al. 2003).

[2] HAWK-I's methane filter avoids the methane absorption found in T and Y dwarfs at 1.6–1.7 μm, meaning T dwarfs appear brighter in CH_4 than H.

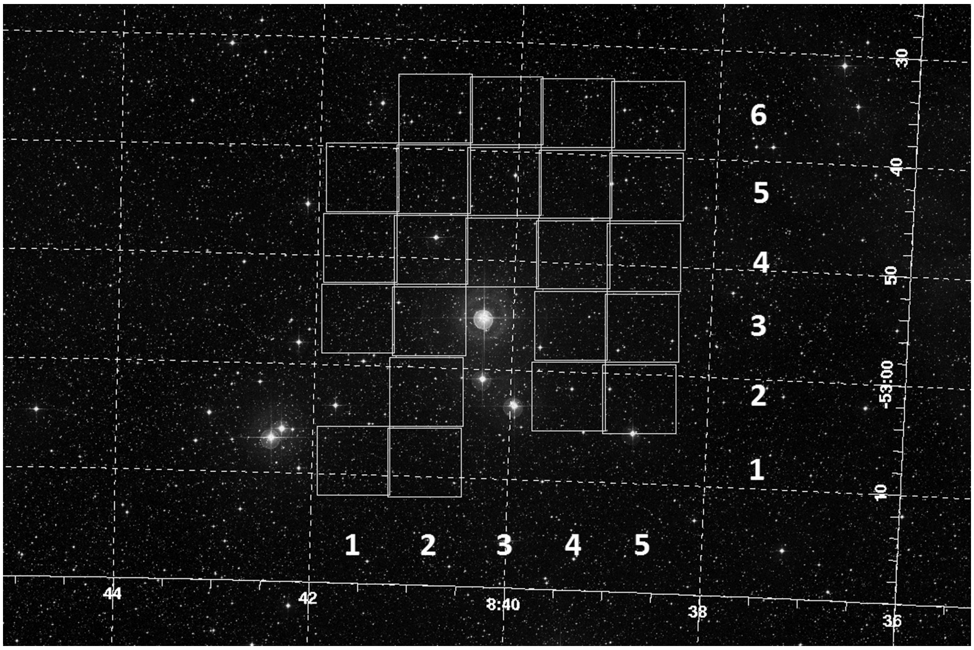

Figure 1. Schematic of IC 2391 showing the 23 overlapping fields observed with HAWK-I. Each field is 7.5 arcmin on a side. Background image is an R plate image from the Anglo-Australian Observatory, taken with the UK Schmidt Telescope and digitized by the STScI for the Digitized Sky Survey at ESO (Version II).

The strength of searching for T dwarfs in the near-infrared using this technique is that no other stars have this strong methane absorption feature (Tinney et al. 2005), allowing surveys containing thousands of objects to be photometrically narrowed to just tens of candidate objects requiring spectroscopic confirmation.

2 PHOTOMETRIC SURVEY

For our survey of IC 2391, infrared imaging was carried out on the nights of 2009 January 15–18, using the High Acuity Wide field K-band Imager (HAWK-I) on the Very Large Telescope (VLT; Kissler-Patig et al. 2008). 23 overlapping pointings (each 7.5 × 7.5 arcmin^2, with a pixel scale of 0.1065 arcsec pixel^{-1}) were observed in conditions of 1.0 arcsec seeing or better (see Fig. 1 and Table 1). Overlap between adjacent pointings was ∼1 arcmin, with dither offsets randomly determined for each exposure, up to a maximum of 30 arcsec in right ascension (RA) and declination (Dec.). HAWK-I is equipped with H and CH_4 filters as shown in Fig. 2. The H filter is centred at 1.620 μm (1.4755–1.7645 μm) while the CH_4 filter is centred at 1.575 μm (1.519–1.631 μm). For each pointing, observations consisted of 16 × 120 s randomly dithered exposures taken in each of the CH_4 and H filters.

2.1 Reduction and photometry

Image processing was performed using PYTHON scripts provided by C. Lidman. In this processing, groups of exposures at each pointing and in each filter were bad pixel masked and dark subtracted prior to flat-fielding and sky subtraction. Dark subtraction was performed by subtracting off a median dark exposure created from all darks of the same integration time. A flat-field for each night was constructed from twilight flats taken at the beginning and end of that night. These flat-fields were applied to each group of exposures for each night, after first masking out detected objects in each image. After flat-fielding, individual exposures were then sky subtracted before being combined to form a mosaic.

Table 1. Field centre coordinates for IC 2391 fields observed with HAWK-I's CH_4 and H passbands, and full width at half-maximum (FWHM) for each field in the final mosaic. Also included is the completeness limit for the CH_4 mosaic.

Field (*x*, *y*)	RA	Dec.	FWHM (arcsec)	CH_4 limit (mag)
1, 1	$08^{h}41^{m}43^{s}.40$	$-53^{\circ}08'44''.1$	0.6	20.9
1, 3	$08^{h}41^{m}42^{s}.96$	$-52^{\circ}55'44''.1$	0.7	20.7
1, 4	$08^{h}41^{m}42^{s}.74$	$-52^{\circ}49'14''.1$	0.9	20.1
1, 5	$08^{h}41^{m}42^{s}.54$	$-52^{\circ}42'44''.1$	0.8	20.3
2, 1	$08^{h}41^{m}00^{s}.05$	$-53^{\circ}08'44''.1$	0.7	20.7
2, 2	$08^{h}40^{m}59^{s}.94$	$-53^{\circ}02'14''.1$	0.7	20.5
2, 3	$08^{h}40^{m}59^{s}.83$	$-52^{\circ}55'44''.1$	0.8	20.3
2, 4	$08^{h}40^{m}59^{s}.72$	$-52^{\circ}49'14''.1$	0.8	20.1
2, 5	$08^{h}40^{m}59^{s}.72$	$-52^{\circ}42'44''.1$	0.7	20.7
2, 6	$08^{h}40^{m}59^{s}.49$	$-52^{\circ}36'14''.1$	0.5	21.1
3, 4	$08^{h}40^{m}16^{s}.70$	$-52^{\circ}49'14''.1$	0.9	19.9
3, 5	$08^{h}40^{m}16^{s}.70$	$-52^{\circ}42'44''.1$	0.8	20.1
3, 6	$08^{h}40^{m}16^{s}.70$	$-52^{\circ}36'14''.1$	0.6	20.9
4, 2	$08^{h}39^{m}33^{s}.46$	$-53^{\circ}02'14''.1$	0.8	20.5
4, 3	$08^{h}39^{m}33^{s}.57$	$-52^{\circ}55'44''.1$	0.6	20.9
4, 4	$08^{h}39^{m}33^{s}.70$	$-52^{\circ}49'14''.1$	0.9	20.3
4, 5	$08^{h}39^{m}33^{s}.78$	$-52^{\circ}42'44''.1$	0.8	20.5
4, 6	$08^{h}39^{m}33^{s}.91$	$-52^{\circ}36'14''.1$	0.5	20.9
5, 2	$08^{h}38^{m}50^{s}.22$	$-53^{\circ}02'14''.1$	1.0	19.9
5, 3	$08^{h}38^{m}50^{s}.44$	$-52^{\circ}55'44''.1$	0.8	20.3
5, 4	$08^{h}38^{m}50^{s}.68$	$-52^{\circ}49'14''.1$	0.8	20.3
5, 5	$08^{h}38^{m}50^{s}.86$	$-52^{\circ}42'44''.1$	0.6	20.9
5, 6	$08^{h}38^{m}51^{s}.12$	$-52^{\circ}36'14''.1$	0.6	20.7

To establish a photometric system for the data, aperture photometry was performed on all the mosaics. Objects in each field were initially located using SEXTRACTOR (Bertin & Arnouts 1996) before

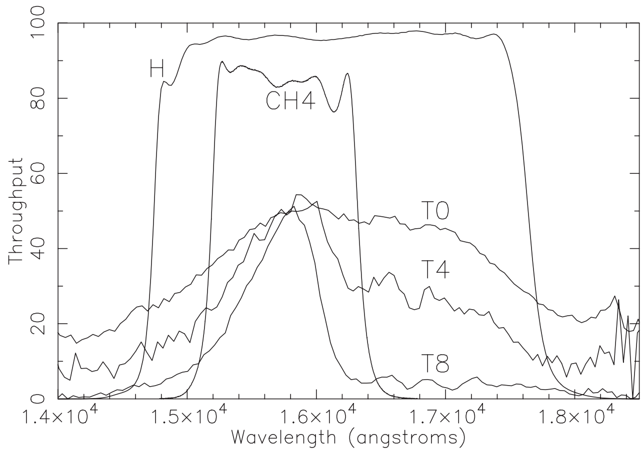

Figure 2. HAWK-I H and CH_4 filter transmission profiles between 14 000 and 18 500 Å. Also plotted are T dwarf spectra (obtained from the SpeX Prism Spectral Libraries online and normalized at 15 800 Å): a T0 (SDSS J1207+0244; Looper, Kirkpatrick & Burgasser 2007), a T4 (2MASS J2151−4853; Burgasser et al. 2006) and a T8 (2MASSI J0415−0935; Burgasser et al. 2004), showing the increasing $CH_4 - H$ trend due to methane absorption.

being photometered using the FIGARO package[3] using a 0.5 arcsec diameter aperture. Zero-points were calculated from Two Micron All Sky Survey (2MASS) stars in each field, transforming them on to the Mauna Kea Observatories (MKO) photometric system (Tokunaga, Simons & Vacca 2002). This transformation was done for 2MASS stars with $J - K$ colours in the range $-0.2 < J - K < +2.4$ (Cutri et al. 2003). For each field, this resulted in a minimum of 20 stars being used for the zero-point calculations – usually the number was between 40 and 50 stars. HAWK-I has linear response to around 30 000 adu, which in our data corresponds to $H = 13.8$ mag. To avoid non-linear effects, zero-points were calculated from 2MASS stars in the range $H = 14.0$–16.5, which had typical uncertainties of 0.001–0.003 mag in the HAWK-I data.

All the 2MASS stars used for this calibration from the above colour range correspond to spectral classes earlier than T. We used this in an analogous way to Tinney et al. (2005) to determine our CH_4 zero-point in addition to our H zero-point, assigning these objects a methane colour ($CH_4 - H$) of zero.

We determined a nominal completeness limit to each field (Table 1), defined as 0.8 mag brighter than the peak of the histogram of objects as a function of their CH_4 magnitude (e.g. Fig. 3). This definition was reached by visually examining objects at the faint end of the histogram to determine if they were real objects or false detections due to spurious detector artefacts or imperfections from the flat fielding process. The limit was then defined as the magnitude at which less than 10 per cent of objects per bin were detector artefacts. These limits varied over the survey, though were consistent within 0.2 mag for any particular seeing.

Additionally, a range of known T dwarfs of varying spectral type (T0–T9) were observed in CH_4 and H to determine a calibration from $CH_4 - H$ to spectral type (Table 2 and Fig. 4). This calibration was parametrized as a quadratic fit, given in equation (1):

$$\text{T subtype} = -0.21 - 18.35\,(CH_4 - H) - 8.63\,(CH_4 - H)^2, \quad (1)$$

where CH_4 and H are objects' magnitudes in those filters, respectively. The root-mean-square (rms) of residuals about the fit is 0.5 for estimated spectral type. The quadratic fit (equation 1 and Fig. 4) is not able to differentiate between spectral types earlier than T0.

2.2 Methane imaging analysis

Detailed analysis of these crowded fields was carried out using the ISIS difference imaging package[4] (Alard 2000). This had advantages over the more straightforward process of detecting and photometering objects in each image separately, as it enabled detection of faint objects that were blended with brighter objects that would otherwise be missed.

Using difference imaging for T dwarf selection does add some complexities. One was that it was possible to select false positives due to transient pixels (e.g. cosmic rays or detector artefacts) in the CH_4 image – such transient pixels would not have H counterparts, and therefore have positive difference fluxes. To avoid this, the individual exposures that created the CH_4 mosaic were also processed in two 'split' groups (i.e. the first half of the exposures in one 'split' and the second half in the other 'split'). Any false positives due to transient pixels then appeared differently in the two splits, and were able to be ruled out.

Additionally, difference imaging produces a flux difference image, rather than a colour. After identifying peaks in the difference image it was therefore necessary to perform photometry at the same position in at least one of the original images so as to convert difference image fluxes into colours. We did this conversion with H photometry as it has a wider bandpass and delivers smaller photometric uncertainties. This conversion is given by equations (2) and (3) below:

$$(\mathrm{CH4} - \mathrm{H})_{\mathrm{diff}} = -2.5\log_{10}\left(\frac{\mathrm{Flux}_{\mathrm{CH_4}}}{\mathrm{Flux}_{\mathrm{H}}}\right) \quad (2)$$

$$= -2.5\log_{10}\left(\frac{\mathrm{Flux}_{\mathrm{diff}}}{\mathrm{Flux}_{\mathrm{H}}} + 1\right), \quad (3)$$

where $(\mathrm{CH4} - \mathrm{H})_{\mathrm{diff}}$ is the colour calculated from the difference image flux, and $\mathrm{Flux}_{\mathrm{CH_4}}$, $\mathrm{Flux}_{\mathrm{H}}$ and $\mathrm{Flux}_{\mathrm{diff}}$ are the object's fluxes in those images, respectively.

We quantified the average uncertainty in the $CH_4 - H$ colour as a function of CH_4 magnitude for each field (denoted $\delta(CH_4 - H)_{CH_4}$ below). This was done by binning all objects in a field into 0.2 mag bins and then averaging the photometric uncertainties within each of these bins. The individual uncertainties for both CH_4 and H were obtained from running SEXTRACTOR on each image.

2.3 Candidate selection

To be selected as a T dwarf candidate, objects had to satisfy several criteria in the object detection algorithm. These criteria are listed below, with the reason for their inclusion given in parentheses at the end of each criterion.

(i) Have a peak in the difference image of at least four connected pixels exceeding 1.5× rms of the sky flux in the difference image. (Potential candidates were required to have significantly non-zero flux in the difference image.)

[3] http://www.aao.gov.au/figaro/

[4] http://www2.iap.fr/users/alard/package.html

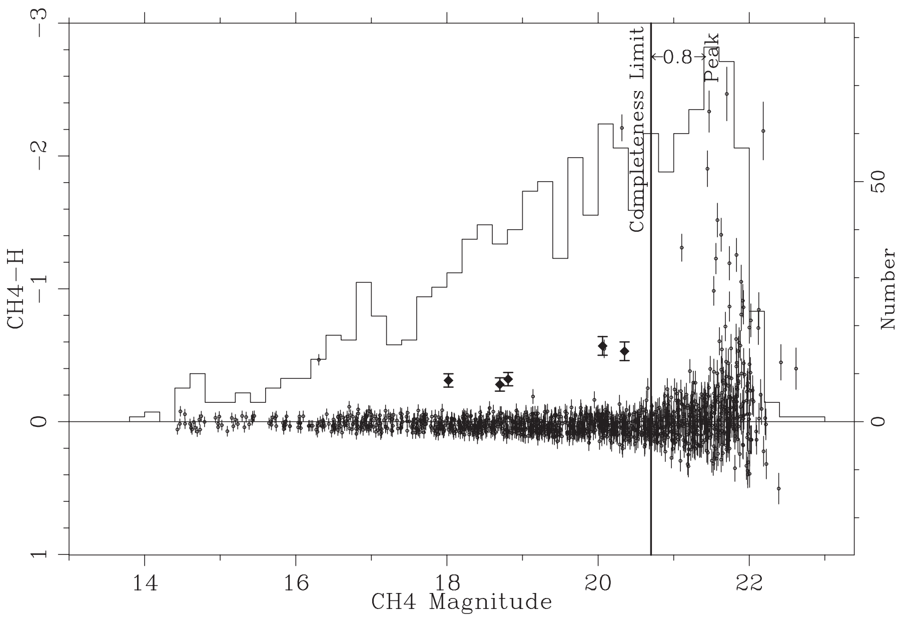

Figure 3. Histogram showing number of objects versus their CH_4 magnitude in 0.2 mag bins, for field 1, 1 (as an example). The thick line is the adopted completeness limit 0.8 mag brighter than the histogram peak for this field. The individual dots are stars in the 1, 1 field on a $CH_4 - H$ versus CH_4 plot. The diamonds are five T dwarf candidates selected from our survey (Section 2.3), though only one actually lies in field 1, 1.

Table 2. T dwarfs observed for spectral type versus $CH_4 - H$ calibration.

T dwarfs	CH_4	H	$CH_4 - H$	SpT
SDSS 0423−0414	13.54 ± 0.02	13.58 ± 0.02	-0.04 ± 0.03	T0
2MASS 1122−3512	14.19 ± 0.02	14.35 ± 0.01	-0.16 ± 0.02	T2
SDSS 1021−0304	15.42 ± 0.03	15.54 ± 0.07	-0.13 ± 0.07	T3
2MASS 1546−3325	15.17 ± 0.02	15.55 ± 0.02	-0.38 ± 0.03	T5.5
2MASS 0243−2453	14.83 ± 0.06	15.22 ± 0.05	-0.39 ± 0.08	T6
2MASS 0348−6022	14.83 ± 0.02	15.42 ± 0.02	-0.58 ± 0.03	T7
2MASS 0415−0935	15.04 ± 0.02	13.58 ± 0.03	-0.67 ± 0.04	T8
CFBDS 0059−0114	17.68 ± 0.06	18.40 ± 0.06	-0.72 ± 0.08	T9

(ii) $(CH_4 - H)_{diff}$ of at least 0.15 mag. (The non-zero flux from the above criterion should correspond to a magnitude difference of at least 0.15 mag – see equations (2) and (3) above.)

(iii) CH_4 at least 0.8 mag brighter than the peak of the CH_4 histogram. (This was to ensure that the completeness limits of our survey remained as high as possible – see Fig. 4 and Section 2.1 for details.)

(iv) $CH_4 - H < -(0.15\ \mathrm{mag} + \delta(CH_4 - H)_{CH_4})$. (To ensure that any candidate's methane colour is significantly non-zero, especially for faint candidates.)

(v) A magnitude difference between splits <0.3 mag. (This was to eliminate false positives due to transient pixels in the CH_4 mosaic. Our photometric uncertainties lie within this limit.)

(vi) FWHM in CH_4 between 0.7 and 2.0 times the median FWHM for that field. (To eliminate some transient pixels [FWHM < 0.7] and extended objects [FWHM > 2.0].)

(vii) Elongation (FWHM semimajor axis/FWHM semiminor axis) in $CH_4 < 2$. (To eliminate non-stellar objects (e.g. galaxies).)

After performing this analysis, a list of five potential candidates was obtained. This list was then checked by eye to ensure that all candidates appeared reasonable as set out by the above criteria. These five candidates (Fig. 5 and Table 3) were then taken to Magellan for spectroscopic follow-up.

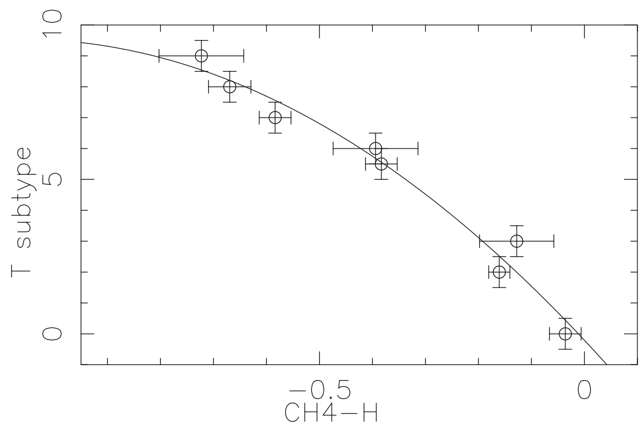

Figure 4. Calibration plot of T subtype versus $CH_4 - H$ colour. The fitted line is given in equation (1). A typical uncertainty of 0.5 was assigned for each spectral type.

3 SPECTROSCOPIC FOLLOW-UP

Spectroscopic follow-up observations of the candidate T dwarfs were carried out on 2011 May 22 and 2012 January 16, using the Folded-port Infrared Echellette (FIRE) spectrograph on Magellan (Simcoe et al. 2008). Two candidates were observed in May, with the remaining three candidates being observed in January. Both runs used FIRE in long-slit mode (R = 300–500), with candidate observations consisting of 120 s exposures before nodding along the slit, using Fowler-2 read mode. Observation specifications for each candidate are shown in Table 4. In May a 1.0-arcsec slit was used to match poor seeing conditions, while in January a 0.6-arcsec slit was used. Immediately before or after each candidate was observed, a bright G-type star was observed at similar airmass, providing a telluric absorption correction. Dark exposures, screen flats and NeAr arc lamp exposures were also taken on both runs

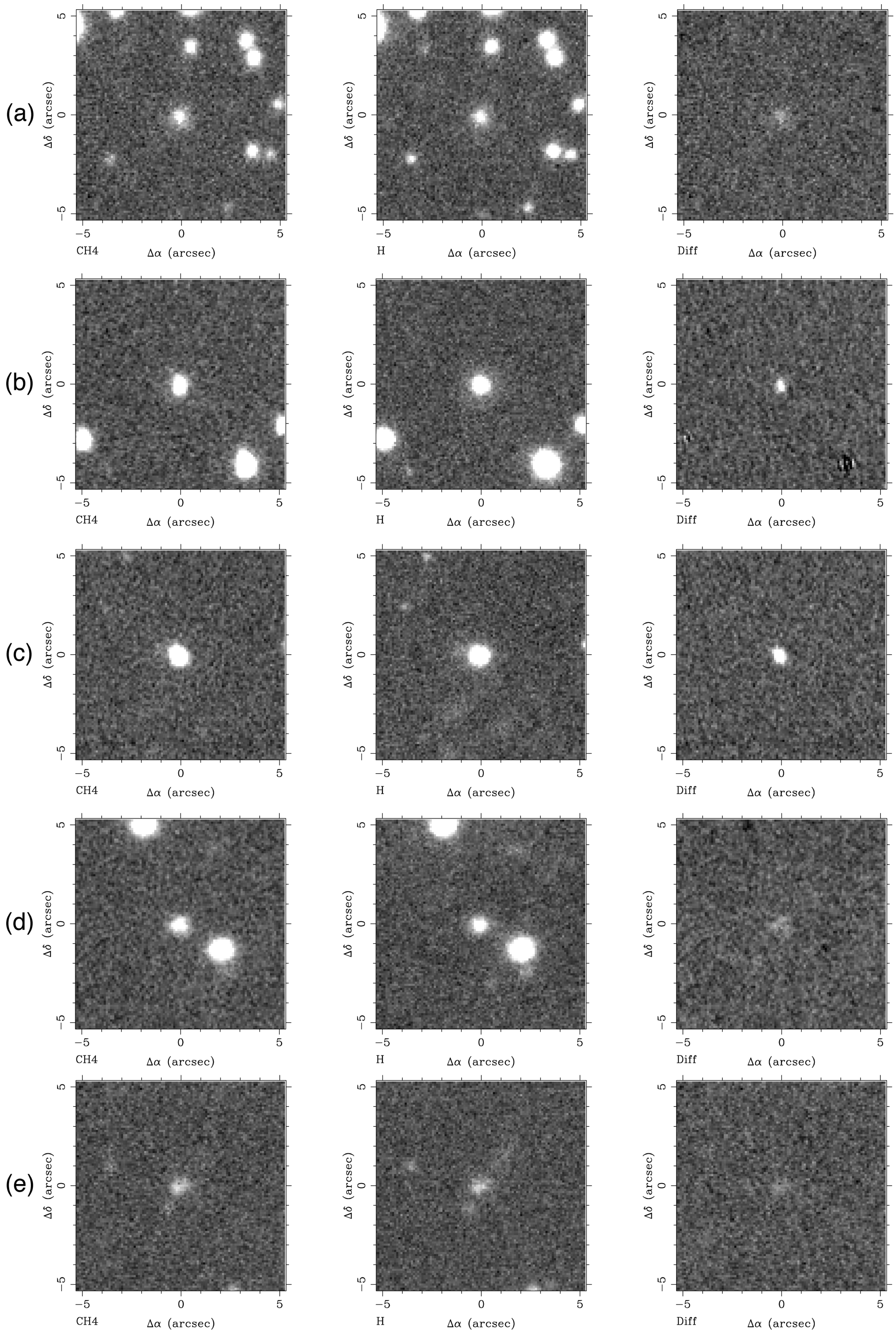

Figure 5. (a)–(e) Candidate finding charts for candidates 1–5, respectively. The first panel is the CH_4 image, the second the H image and the third the difference image, all on the same stretch.

during the day. Lastly, twilight flats were taken on both runs during morning and evening twilight.

Reduction of the data was performed using routines from the FIGARO package, modified to correctly propagate uncertainties.

First, error arrays were created for all the images using the nominal read noise, gain and photon counts in each pixel.

Second, a bad pixel mask was generated that flagged hot, dead and poorly flattening pixels, which was then applied to all the images.

Table 3. Candidate properties.

Number	Field (x, y)	RA	Dec.	CH_4	H	$CH_4 - H$	SpT(est.)
1	1, 1	$08^h41^m39\overset{s}{.}19$	$-53°06'56\overset{''}{.}2$	20.06 ± 0.04	20.63 ± 0.05	-0.57 ± 0.07	T7.5
2	2, 6	$08^h41^m17\overset{s}{.}63$	$-52°34'57\overset{''}{.}7$	18.81 ± 0.03	19.12 ± 0.03	-0.32 ± 0.05	T5
3	2, 6	$08^h40^m41\overset{s}{.}09$	$-52°33'07\overset{''}{.}5$	18.02 ± 0.03	18.33 ± 0.04	-0.31 ± 0.05	T4.5
4	3, 4	$08^h39^m55\overset{s}{.}96$	$-52°46'08\overset{''}{.}0$	18.70 ± 0.04	18.97 ± 0.03	-0.28 ± 0.05	T4
5	5, 6	$08^h39^m05\overset{s}{.}61$	$-52°38'14\overset{''}{.}1$	20.35 ± 0.05	20.88 ± 0.05	-0.53 ± 0.07	T7

Table 4. Candidate spectroscopic observation specifications.

Number	Date observed	Seeing (arcsec)	Exposure length (s)
1	2012 January 16	0.6	2880
2	2011 May 22	2.0	1440
3	2011 May 22	3.0	960
4	2012 January 16	0.7	960
5	2012 January 16	0.6	3120

Dead pixels were defined as 10σ outliers in an rms map of pair subtracted dark exposures. Hot and poorly flattening pixels were flagged by hand after applying the dead pixel mask to the twilight flat exposures.

Third was dark subtraction followed by application of a flat-field created from dome flats.

Fourth, the data underwent a correction for non-uniform slit throughput. Twilight flats were straightened in both directions by tracing lines in an arc lamp exposure (for straightening in the spatial dimension), as well as tracing bright stars in the slit (for straightening the wavelength dimension). Straightened twilight flats then had ~10 wavelength-pixel sections collapsed to produce slit throughput profiles at three wavelength positions across the detector. These throughput profiles were made along telluric lines at pixels ~420, 1050 and 1790, to ensure high counts on the detector. These profiles were visually inspected, and showed the same non-uniform but smooth throughput at all positions. The entire spectrum for each twilight flat was then collapsed along the wavelength direction and normalized by the median of the central 150 pixels. A fifth-order polynomial was fitted to the average of these collapsed twilight flats, before being re-interpolated back along the wavelength axis and divided out from the arc, telluric and target images. The overall correction for the non-uniformity in slit illumination was less than 2 per cent.

Fifth, images were straightened along both axes (in the same fashion as the twilight flats above) so that spectra could be extracted. Before extracting spectra, individual exposures in the same position along the slit were averaged, weighted by their variance arrays. After extracting each of these positions separately, their resulting spectra were then averaged to create a final single spectrum for each object.

Sixth, final combined spectra were wavelength calibrated using a NeAr arc lamp spectrum taken earlier during the day. This arc spectrum was processed in the same manner as the data, and extracted from the same pixels. A relative wavelength calibration was difficult to reach and we were forced to omit wavelengths below 0.96 µm (due to few lines below this wavelength and the highly non-linear wavelength-to-pixel relation). Spectra were then examined for any signs of cosmic rays. Any potential cosmic rays had their corresponding positions checked in the individual flattened images, and if real, were flagged as bad by hand. Only three cosmic rays were removed in this fashion across all candidate and telluric spectra.

Finally, the spectra underwent a relative flux calibration, dividing by the corresponding normalized telluric observation and then multiplying by a normalized blackbody of the same temperature as the telluric. Resulting spectra from May were then re-binned by a factor of 6, and by a factor of 2 for January. This resulted in final spectral resolutions of ~70 and ~200, respectively, with a final signal-to-noise ratio of ~8–10 pixel^{-1}.

4 RESULTS

The final re-binned spectra are shown in Fig. 6. It is clear that all candidates can be ruled out as T dwarfs. Four of the five candidate spectra show obvious emission lines that fall within the CH_4 band-pass and which would therefore trigger a methane signature, while the fifth object is likely a background star scattered into our photometric selection criteria. Lines identified and estimated redshifts[5] for the candidates are shown in Table 5.

To test whether the observed spectra were consistent with the $CH_4 - H$ colour by which objects were originally selected, we calculated synthetic $CH_4 - H$ colours from their spectra by multiplying them by the HAWK-I CH_4 and H filter profiles[6] and then converting the corresponding fluxes into a colour. A relative zero-point between the H and CH_4 filters for this synthetic colour was calculated from a model spectrum of Vega[7] by measuring its flux in both filters and assigning it a colour of zero. It should be stressed that the synthetic colours have large uncertainties resulting from the low signal-to-noise ratio. A comparison between measured HAWK-I colour and this synthetic FIRE colour is shown in Table 6. All are consistent within the uncertainties.

We conclude that no T dwarfs are present in our methane imaging survey volume of IC 2391. While this is disappointing from the point of view of identifying T dwarfs, it is encouraging that our methane imaging analysis has correctly selected astrophysical sources with spectra demonstrating an equivalent $CH_4 - H$ signature. These results highlight the *need* for spectroscopic confirmation of candidates selected by photometric selection criteria.

5 DISCUSSION

As with all searches for rare astrophysical objects, care needs to be taken with contamination. For a survey such as ours, there were a few advantages in this aspect. First, the compact size of a cluster as a place to search for methane objects means that foreground contamination is incredibly unlikely, as field T dwarfs are much older and fainter, and only detectable out to ~50 pc. For the area our survey covered, the space densities

[5] Identification from comparison with composite quasar spectra of Tinney, Da Costa & Zinnecker (1997).

[6] Available from http://www.eso.org/sci/facilities/paranal/instruments/hawki/inst/

[7] The same one as used by Tokunaga & Vacca (2005): http://kurucz.harvard.edu/stars/VEGA

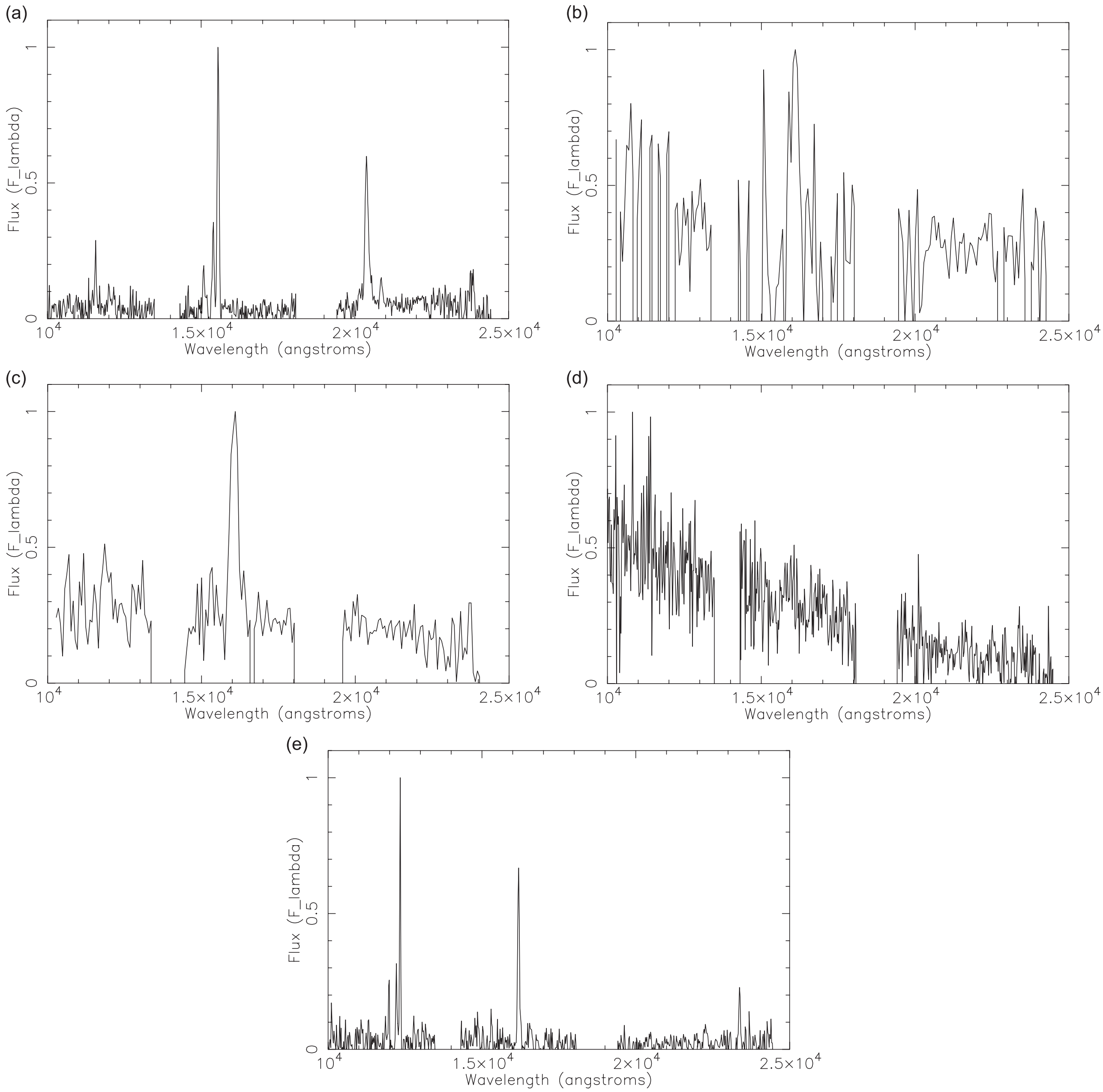

Figure 6. (a)–(e) Spectra of candidates 1–5, observed with FIRE on Magellan. Spectra are on an arbitrary $f(\lambda)$ flux scale.

Table 5. Candidate line identification and redshifts.

Number	Identified lines	Redshift
1	Hα, O III	2.104 ± 0.006
2	Hα	1.453 ± 0.013
3	Hα	1.451 ± 0.022
4	None	–
5	Hα, O III	1.465 ± 0.004

of Kirkpatrick et al. (2011) predict 0.02 foreground T dwarfs in our whole survey. Furthermore, as there is no such thing as a 'methane giant', our survey should be robust against background contamination.

5.1 Evolutionary models

To determine if the absence of T dwarfs in IC 2391 is due to an actual absence in the cluster, or just a lack of sensitivity in our survey, we calculated the expected magnitudes that we would expect T dwarfs to have in IC 2391. This was performed using the BT-Settl evolutionary models of Allard, Homeier & Freytag (2012), accessed through the PHOENIX web simulator.[8]

To calculate the expected H magnitude of potential T dwarfs and therefore determine at what magnitudes we can detect their methane absorption, the HAWK-I filter profiles were uploaded to PHOENIX which returned their $CH_4 - H$ colour as a function of effective temperature and surface gravity. This was combined with a

[8] http://phoenix.ens-lyon.fr/simulator/index.faces

Table 6. Candidate colour comparison.

Number	Photometric				Synthetic		Field CH_4	Re-detection
	CH_4	H	$CH_4 - H$	SpT	$CH_4 - H$	SpT	completeness	rate (per cent)
1	20.06 ± 0.04	20.63 ± 0.05	-0.57 ± 0.07	T7.5	-0.54 ± 0.10	T7	20.9	86
2	18.81 ± 0.03	19.12 ± 0.03	-0.32 ± 0.05	T5	-0.13 ± 0.14	T2	21.1	86
3	18.02 ± 0.03	18.33 ± 0.04	-0.31 ± 0.05	T4.5	-0.24 ± 0.16	T3.5	21.1	81
4	18.70 ± 0.04	18.97 ± 0.03	-0.28 ± 0.05	T4	-0.04 ± 0.10	T0.5	19.9	70
5	20.35 ± 0.05	20.88 ± 0.05	-0.53 ± 0.07	T7	-0.35 ± 0.11	T5	20.7	53

Table 7. Expected apparent H magnitude and CH_4 − H colour for a range of brown dwarf temperatures for 50 Myr old T dwarfs from PHOENIX.

T_{eff}	$\log g$	H	$M/\mathrm{M}_{\odot}$	$CH_4 - H$	SpT[a]
1400	4.24	18.41	0.011	+0.08	T0
1300	4.23	18.78	0.011	+0.05	T0
1200	4.23	19.14	0.010	+0.00	T0
1100	4.20	19.58	0.009	−0.06	T1
1000	4.13	20.10	0.008	−0.21	T3
900	4.06	20.77	0.007	−0.39	T5.5
800	3.97	21.56	0.006	−0.52	T7
700	3.87	22.41	0.004	−0.67	T8
600	3.74	23.34	0.003	−0.78	T9

[a]Based on equation (1) from Section 2.1.

pre-existing MKO filter set 50 Myr isochrone at solar metallicity for brown dwarfs of temperatures 600–1400 K.[9] This pre-existing isochrone (available on the PHOENIX website) contained the relation between effective temperature, surface gravity and absolute H magnitude. By linearly interpolating between the model values of both temperature and gravity, the apparent H versus CH_4 − H relation in Table 7 was derived. This model supports the magnitude–spectral type relation from Table 2, as well as showing few fields were complete to expected T dwarf magnitudes (Tables 1 and 7).

5.2 Simulations

To interpret our methane imaging results, we simulated our data by injecting fake T dwarfs into the images, seeing how many were successfully re-selected and looking at the statistics of a large number of such simulations.

The first step in preparing these simulations was measuring a point spread function (PSF) for each image (CH_4, H and each split). This was done using the DAOPHOT software package (Stetson 1987, as implemented in the STARLINK environment).[10] DAOPHOT was used to select bright, unsaturated stars in each field to measure the PSF. This list was verified by eye to remove blended stars and stars close to the edge of an image. The final PSF fitted was a Moffat function plus a residual PSF correction, measured over a radius of 70 pixels.

Next, the zero-point offset between fake stars added by DAOPHOT with this PSF, and that measured by aperture photometry (which was used in the candidate selection algorithm – see Section 2), was determined. This was done by adding 20 stars to a blank image, for magnitudes in the range 18.0–23.5 in 0.25 mag intervals, before doing aperture photometry on them. The difference recovered was constant across this magnitude range to within 0.02 mag, and was implemented as a single zero-point correction to all the DAOPHOT magnitudes.

Next, a set of 30 random pixel coordinates was generated over the entire field, as well as a randomly selected H magnitude from the range 18.0 to 23.5 in 0.25 mag intervals, and a randomly selected CH_4 − H colour from the values of −0.1, −0.2, −0.3, −0.4, −0.5, −0.6, −0.7 and −0.8. These colours correspond to T dwarfs of type T1.5–T9. This range of magnitudes and colours was chosen to measure the detection sensitivity of our method independent of the expected T dwarf apparent magnitudes from the evolutionary model (Section 5.1). These coordinates, magnitudes and colours were used to add fake T dwarfs into copies of the real data. These 'fake' images were then reprocessed through the same difference imaging scripts as the real data. The same object detection script as before was then run on the fake-injected images.

After the detection script was run, a comparison of injected fakes with re-detected fakes was performed, outputting a final list containing the parameters of each injected star, and whether it was successfully re-detected. This was repeated 400 times for each field for a total of 12 000 injected T dwarfs per field. The result is a plane of object detection rate as a function of H and CH_4 − H for each field.

There was some field-to-field variation in detection sensitivities. Fig. 7 shows example plots of these planes, for our best (2, 6) and worst (5, 5) fields. In our best fields, we were sensitive to detecting some T-type dwarfs at their expected IC 2391 luminosities, while in most of our fields we had little to no sensitivity to detecting T dwarfs at their expected luminosities.

To quantify the sensitivity of each field, we compared their magnitude depths with the expected magnitudes of T dwarfs in the cluster (Table 8). The value used for this depth calculation was the 50 per cent detection rate for $CH_4 - H = -0.3$, as compared with the interpolated model prediction of $H = 20.44$ for a distance of 146 pc. This colour was chosen as the measure of sensitivity as a priori we were not expecting to be sensitive to smaller colours, and therefore this colour would correspond to the brightest T dwarfs we could expect to find.

The distance to which each field probed was calculated from the magnitude depth. This was compared with the distance range expected for the cluster and used to derive a weight for each field based on the volume of the cluster it probed. A radius of 3.19 pc was adopted for the cluster, calculated from Kharchenko et al. (2005), placing the cluster edges at distances of 142.8 and 149.2 pc, respectively. Weights were assigned to each field assuming that they probed with a uniform cross-section into the cluster. The weights were assigned such that fields that did not probe deep enough to see the cluster were given a weight of 0 and fields that probed through the cluster were given a weight of 1. Fields that partially probed the cluster were assigned a weight within this range, based on the volume of the cluster they probed (Table 8).

[9] Based on known T dwarf effective temperatures (Vrba et al. 2004).
[10] http://starlink.jach.hawaii.edu/starlink

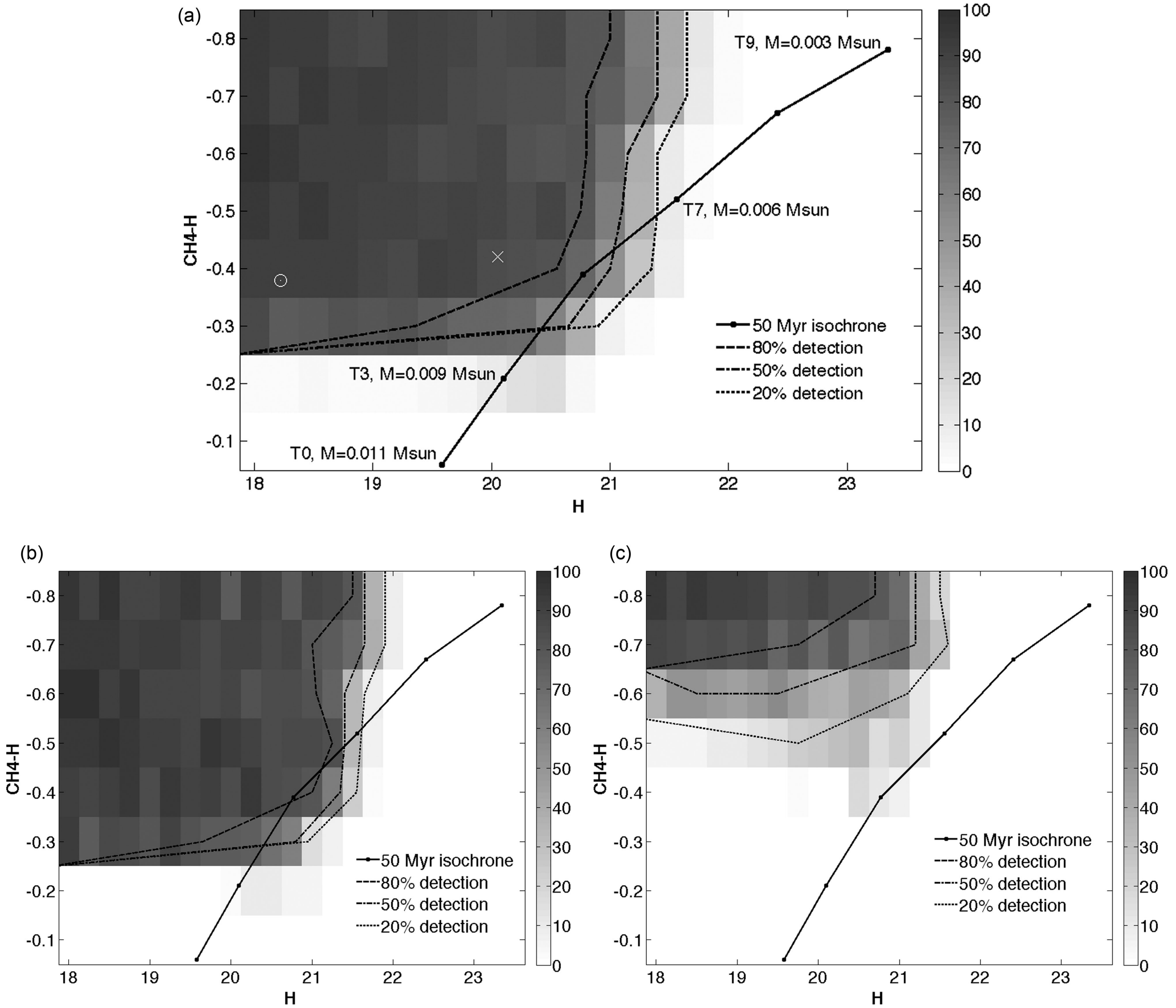

Figure 7. Detection rate for different IC 2391 fields for simulated T dwarfs. (a) Shows the weighted detection rates for all fields from Table 8, (b) shows detection rates for our best field (2, 6) and (c) shows detection rates for our worst field (5, 5). Also shown are the 50 Myr isochrone from the BT-Settl model of Allard et al. (2012) (solid line), as well as the 80, 50 and 20 per cent detection rates for each sample (dashed, dot–dashed and dotted lines, respectively). Lastly, two known T dwarfs that potentially lie within other young clusters are shown in panel (a): σ Ori 70 from Zapatero Osorio et al. (2002) (T5.5, 1–8 Myr, circle) and IC348_CH$_4$_2 from Burgess et al. (2009) (T6, 3 Myr, $\times$), shifted to the 146 pc distance of IC 2391.

The weighting calculation showed that most fields observed did not probe deep enough to reach the cluster, with only four fields probing deep enough to see IC 2391. This agreed with the results from comparing the field completeness limits with expected T dwarf magnitudes from the evolutionary model (Tables 1 and 7). Finally, these weights were used to average the detection rates across all fields, shown in Fig. 7.

For the weighted detection rate (Fig. 7 and Table 9), brighter stars with a larger $CH_4 - H$ colour were easier to detect, while early-type T dwarfs were nearly impossible to find. Importantly, these simulations showed that in the fields that reached the cluster, we were sensitive to detecting a high percentage of T dwarfs down to faint magnitudes. Limiting magnitudes for the 80, 50 and 20 per cent detection rate contours as a function of $CH_4 - H$ are given in Table 9.

Combining Tables 7 and 9, an expected H magnitude versus detection rate as a function of spectral type was derived, shown in Table 10. This shows that we were mainly able to detect T dwarfs of spectral types T4–T6.

5.3 Mass function

From Table 9, we can determine what limits our non-detection of T dwarfs can place on possible mass functions for IC 2391. First, known IC 2391 cluster members from Barrado y Navascués et al. (2001) were used to create a cluster mass function (Fig. 8) for the known members in their $\sim$2.5 deg^2 survey. Cluster masses were calculated from the mass–magnitude relation in the BT-Settl 50 Myr isochrone (Section 5.1). This mass function can then be parametrized in two separate ways: first by fitting a log-normal function (equation 4); and secondly by fitting a split power-law function of the form $dN/dM \propto M^{-\alpha}$ (equations 5 and 6). For both these parametrizations, dN/dM represents the number of stars per

Table 8. Depth probed for each field in our survey and corresponding assigned weight. Most fields did not probe deep enough to see the cluster.

Field (*x*, *y*)	FWHM (arcsec)	Depth (mag)	Distance (pc)	Cluster probed?	Weight
1, 1	0.6	20.75	154.7	Yes	1.00
1, 3	0.7	20.30	139.4	No	0.00
1, 4	0.9	20.00	130.1	No	0.00
1, 5	0.8	19.85	125.7	No	0.00
2, 1	0.7	20.40	142.7	No	0.00
2, 2	0.7	20.40	142.7	No	0.00
2, 3	0.8	19.50	117.3	No	0.00
2, 4	0.8	19.90	127.2	No	0.00
2, 5	0.7	20.30	139.4	No	0.00
2, 6	0.5	20.90	160.1	Yes	1.00
3, 4	0.9	19.60	118.7	No	0.00
3, 5	0.8	19.60	118.7	No	0.00
3, 6	0.6	20.60	149.4	Yes	1.00
4, 2	0.8	20.20	136.3	No	0.00
4, 3	0.6	20.35	141.0	No	0.00
4, 4	0.9	20.20	136.3	No	0.00
4, 5	0.8	20.30	139.4	No	0.00
4, 6	0.5	20.55	147.7	Yes	0.76
5, 2	1.0	19.20	109.5	No	0.00
5, 3	0.8	19.95	128.6	No	0.00
5, 4	0.8	19.50	117.3	No	0.00
5, 5	0.6	19.10	107.0	No	0.00
5, 6	0.6	20.35	141.0	No	0.00

Table 9. Weighted average limiting H magnitudes for different detection rates for all fields.

$CH_4 - H$	80 per cent (mag)	50 per cent (mag)	20 per cent (mag)
−0.1	–	–	–
−0.2	–	–	–
−0.3	19.35	20.65	20.9
−0.4	20.55	21.0	21.35
−0.5	20.75	21.1	21.4
−0.6	20.8	21.15	21.4
−0.7	20.8	21.4	21.65
−0.8	21.0	21.4	21.65

square degree in the cluster (d*N*), per mass interval (d*M*) (taken from Barrado y Navascués et al. 2001):

$$\log\left(\frac{\mathrm{d}N}{\mathrm{d}M}\right) = 0.61 - 2.47\,\log(M) - 1.08\,(\log(M))^2, \tag{4}$$

$$\alpha = \ \ 1.7 \pm 0.4, \quad 0.13 < \frac{M}{\mathrm{M}_\odot} < 1.0, \tag{5}$$

$$\alpha = -1.5 \pm 0.6, \quad 0.003 < \frac{M}{\mathrm{M}_\odot} < 0.13. \tag{6}$$

Both the log-normal and split power-law function fits are reasonable approximations to the shape of the mass function in the region where it is well constrained.

These functions were then extrapolated down to expected T dwarf masses (from Table 7). The log-normal extrapolation predicts 0.03 T dwarfs per square degree within the cluster and the power-law extrapolation predicts 0.02. These would correspond to 0.002 and 0.001 objects in the four fields of our survey that are sensitive to

Table 10. Weighted average detection rates for T dwarfs at their expected H magnitude.

Spectral type	$CH_4 - H$	Expected H (mag)	Detection rate (per cent)
T2	−0.13	19.82	2
T3	−0.19	20.03	10
T4	−0.26	20.29	50
T5	−0.34	20.58	63
T6	−0.42	20.95	58
T7	−0.52	21.56	8
T8	−0.64	22.24	0
T9	−0.80	23.51	0

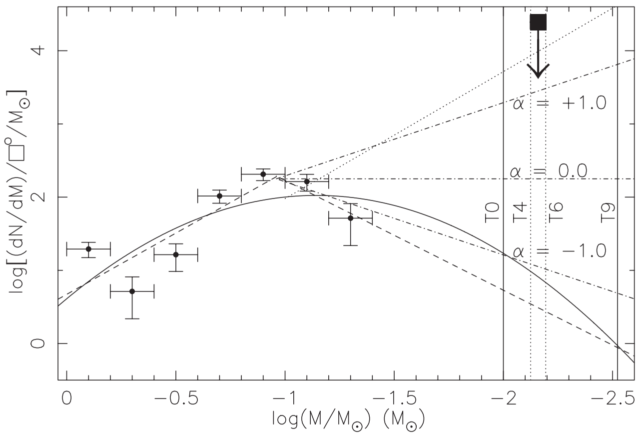

Figure 8. Mass function of IC 2391, showing number of members per mass interval for the survey of Barrado y Navascués et al. (2001). The horizontal error bars show the width of the histogram bins for the mass function (each logarithmic bin has a width of 0.2), the vertical error bars show counting uncertainties. Also shown are a log-normal fit to the data (solid line), a split power-law fit to the data (dashed line), an extrapolated upper limit power law from this paper (dotted line) and three extrapolations of the split power law with $\alpha = +1.0$, 0.0 and −1.0, respectively (dot–dashed lines). The large square represents a single T dwarf within our survey, used in calculating our upper limit. Lastly, expected T dwarf masses are shown for both the entire T range (T0–T9, solid vertical lines) and the T dwarfs we were sensitive to detecting (T4–T6, dotted vertical lines).

T dwarfs. Both of these extrapolations are consistent with our non-detections.

An alternative way in which to interpret our non-detection of T dwarfs is to use it to calculate the upper limit that we could place on a split power-law extrapolation down to T dwarf masses. This requires the extrapolation of the second part of the split power law to predict a number of T dwarfs in the cluster large enough that we would expect to see at least one in our survey. There was a factor of 40 in the difference in cluster area probed by our survey versus that of Barrado y Navascués et al. (2001) (i.e. as our survey was for an effective area of four HAWK-I fields, or 0.0625 deg^2). The upper limit that we derived in this fashion was $\alpha < 1.7$ for masses in the range 0.003–0.13 $\mathrm{M}_\odot$.

6 CONCLUSION

None of the five candidates uncovered by our survey is actually T dwarfs. Four exhibit emission lines in their spectra that led to their selection, with the last object showing no obvious spectral feature that would have led to a $CH_4 - H$ signature.

We expected little contamination from either foreground or background stellar objects to the cluster for our methane imaging survey of IC 2391. However, emission line contaminants due to background galaxies were still present, as demonstrated by the spectra of our candidates. This demonstrates that spectroscopic confirmation is absolutely essential for confirming the nature of any candidates from a methane imaging survey, even if the number of candidates selected from such a survey is substantially less than from a similar *JHK*-selected survey (Tinney et al. 2005). Caution is therefore recommended in interpreting the results of previous surveys without such spectroscopy for their candidates (Mainzer & McLean 2003; Burgess et al. 2009; Goldman et al. 2010; Haisch, Barsony & Tinney 2010; Casewell et al. 2011; Peña Ramírez et al. 2011; Spezzi et al. 2012), though surveys that use more narrow-band filters should be less susceptible to this type of contaminant (e.g. Mainzer & McLean 2003).

A mass function for known IC 2391 members was constructed, and found to be consistent with both log-normal and split power-law parametrizations. Both of these parametrizations were also consistent with zero T dwarfs detected by us in IC 2391. Both parametrizations of the mass function had a turn over at around 0.07–0.16 $M_\odot$, consistent with the value of Boudreault & Bailer-Jones (2009) of 0.13 ± 0.03 $M_\odot$.

Our survey places an upper limit on the low-mass end of IC 2391's mass function of $\alpha < 1.7$ for masses in the range 0.003–0.13 $M_\odot$, excluding Salpeter-like power-law extrapolations ($\alpha = 2.35$). This is consistent with mass functions calculated for other young clusters such as the Pleiades ($\alpha = 1.0 \pm 0.5$ for masses 0.04–0.4 $M_\odot$; Martin, Zapatero Osorio & Rebolo 1998), ρ Ophiuchus ($\alpha = 1.14$ to masses below 0.08 $M_\odot$; Comeron et al. 1993) and σ Orionis ($\alpha = 0.8 \pm 0.4$; Béjar et al. 2001). From the younger age of IC 2391 (50 Myr), we would expect its mass function to be similar to a Pleiades-like mass function – dynamical evolution resulting in the ejection of low-mass cluster members should not have had enough time to significantly deplete their number, as opposed to an older cluster like the Hyades (Bouvier et al. 2008).

Simulations of our data set indicate that we are insensitive to early ($CH_4 - H > -0.3$, ∼T0–T3) or late ($CH_4 - H < -0.5$, ∼T7–T9) type T dwarfs, but are sensitive to mid range T dwarfs ($-0.3 < CH_4 - H < -0.5$, ∼T4–T6), for the luminosities they are expected to have in IC 2391.

These simulations show that a future survey of IC 2391 would need to probe to a depth of $H = 21.8$ at $CH_4 - H = -0.6$ to be able to reliably detect T4–T7.5 dwarfs. In typical good seeing on an 8-m telescope (0.6 arcsec) such a survey would need to cover an area of 0.2 or 1.95 deg^2 (13 and 125 HAWK-I fields) to detect one T dwarf assuming power-law extrapolations of $\alpha = +1.0$ and 0.0, respectively. Assuming a similar distribution of seeing conditions as our 4 d observing run with HAWK-I, this would require observation of 26 and 250 fields.

Any future T dwarf discoveries within IC 2391 will have a profound impact on the shape of its mass function, as they shall likely confirm a Pleiades-like mass function extends below the deuterium burning limit of 0.012 $M_\odot$.

ACKNOWLEDGMENTS

Australian access to the Magellan Telescopes was supported through the National Collaborative Research Infrastructure Strategy of the Australian Federal Government.

REFERENCES

Alard C., 2000, A&AS, 144, 363
Allard F., Hauschildt P. H., Alexander D. R., Tamanai A., Schweitzer A., 2001, ApJ, 556, 357
Allard F., Homeier D., Freytag B., 2012, R. Soc. Lond. Philos. Trans. Ser. A, 370, 2765
Baraffe I., Chabrier G., Barman T. S., Allard F., Hauschildt P. H., 2003, A&A, 402, 701
Barrado y Navascués D., Stauffer J. R., Patten B. M., 1999, ApJ, 522, L53
Barrado y Navascués D., Stauffer J. R., Briceño C., Patten B., Hambly N. C., Adams J. D., 2001, ApJS, 134, 103
Barrado y Navascués D., Stauffer J. R., Jayawardhana R., 2004, ApJ, 614, 386
Béjar V. J. S. et al., 2001, ApJ, 556, 830
Bertin E., Arnouts S., 1996, A&AS, 117, 393
Boss A. P., Basri G., Kumar S. S., Liebert J., Martín E. L., Reipurth B., Zinnecker H., 2003, in Martín E., ed., Proc. IAU Symp. 211, Brown Dwarfs. Astron. Soc. Pac., San Francisco, p. 529
Boudreault S., Bailer-Jones C. A. L., 2009, ApJ, 706, 1484
Bouvier J. et al., 2008, A&A, 481, 661
Burgasser A. J., McElwain M. W., Kirkpatrick J. D., Cruz K. L., Tinney C. G., Reid I. N., 2004, AJ, 127, 2856
Burgasser A. J., Geballe T. R., Leggett S. K., Kirkpatrick J. D., Golimowski D. A., 2006, ApJ, 637, 1067
Burgess A. S. M., Moraux E., Bouvier J., Marmo C., Albert L., Bouy H., 2009, A&A, 508, 823
Casewell S. L., Jameson R. F., Burleigh M. R., Dobbie P. D., Roy M., Hodgkin S. T., Moraux E., 2011, MNRAS, 412, 2071
Chabrier G., Baraffe I., Allard F., Hauschildt P., 2000, ApJ, 542, 464
Comeron F., Rieke G. H., Burrows A., Rieke M. J., 1993, ApJ, 416, 185
Cutri R. M. et al., 2003, Explanatory Supplement to the 2MASS All Sky Data Release. Caltech, Pasadena
Goldman B., Marsat S., Henning T., Clemens C., Greiner J., 2010, MNRAS, 405, 1140
Haisch K. E. Jr, Barsony M., Tinney C., 2010, ApJ, 719, L90
Kharchenko N. V., Piskunov A. E., Röser S., Schilbach E., Scholz R. D., 2005, A&A, 438, 1163
Kirkpatrick J. D. et al., 2011, ApJS, 197, 19
Kirkpatrick J. D. et al., 2012, ApJ, 753, 156
Kissler-Patig M. et al., 2008, A&A, 491, 941
Liu M. C. et al., 2011, ApJ, 740, L108
Looper D. L., Kirkpatrick J. D., Burgasser A. J., 2007, AJ, 134, 1162
Lucas P. W. et al., 2010, MNRAS, 408, L56
Mainzer A. K., McLean I. S., 2003, ApJ, 597, 555
Martín E. L., Zapatero Osorio M. R., Rebolo R., 1998, in Martín E. L., Zapatero Osorio M. R., Rebolo R. ASP Conf. Ser. Vol. 134, Brown Dwarfs and Extrasolar Planets. Astron. Soc. Pac., San Francisco, p. 507
Peña Ramírez K., Zapatero Osorio M. R., Béjar V. J. S., Rebolo R., Bihain G., 2011, A&A, 532, A42
Robichon N., Arenou F., Mermilliod J. C., Turon C., 1999, A&A, 345, 471
Rolleston W. R. J., Byrne P. B., 1997, A&AS, 126, 357
Simcoe R. A. et al., 2008, Proc. SPIE, 7014, 27
Spezzi L., Alves de Oliveira C., Moraux E., Bouvier J., Winston E., Hudelot P., Bouy H., Cuillandre J. C., 2012, A&A, 545, A105
Stetson P. B., 1987, PASP, 99, 191
Tinney C. G., Da Costa G. S., Zinnecker H., 1997, MNRAS, 285, 111
Tinney C. G., Burgasser A. J., Kirkpatrick J. D., McElwain M. W., 2005, AJ, 130, 2326
Tokunaga A. T., Vacca W. D., 2005, PASP, 117, 421
Tokunaga A. T., Simons D. A., Vacca W. D., 2002, PASP, 114, 180
Vrba F. J. et al., 2004, AJ, 127, 2948
Zapatero Osorio M. R., Béjar V. J. S., Martín E. L., Rebolo R., Barrado y Navascués D., Mundt R., Eislöffel J., Caballero J. A., 2002, ApJ, 578, 536

This paper has been typeset from a TEX/LATEX file prepared by the author.